Engineering Structures 241 (2021) 112426

Contents lists available at ScienceDirect

Engineering Structures

journal homepage: www.elsevier.com/locate/engstruct

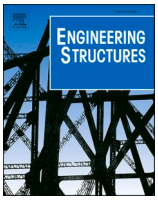

Modelling of earthquake-induced pounding between adjacent structures with a non-smooth contact dynamics method

T. Langlade [a,*], D. Bertrand [a], S. Grange [a], G. Candia [b], J.C. de la Llera [c]

[a] Laboratory GEOMAS EA7495, INSA Lyon, Villeurbanne, France
[b] Research Center for Integrated Disaster Risk Management (CIGIDEN), ANID/FONDAP/15110017, Facultad de Ingeniería, Universidad Del Desarrollo, Santiago de Chile, Chile
[c] Research Center for Integrated Disaster Risk Management (CIGIDEN), Pontificia Universidad Catolica de Chile, Santiago de Chile, Chile

ARTICLE INFO

Keywords:
Earthquake
Building-pounding
NSCD method
Experimental campaign
Contact algorithm
Sensitivity analysis

ABSTRACT

This article presents the kinematic analysis of two adjacent structures with pounding using the framework of finite element dynamic analysis and a non-smooth contact dynamics (NSCD) method for treating contact-impact. The latter consists of a Moreau-Jean implicit integration scheme that uses Moreau's sweeping process and Newton's impact law. Test cases are carried out to prove the efficiency of the implementation and accuracy of the results relative to the widely used penalty method (PM). Furthermore, finite element simulations are compared with shaking table results of two structures susceptible to pounding. Models are steel frames 2.5 m to 5 m high, 3 m in span, have reinforced-concrete slabs, and distant 0 to 5 cm. Floor displacements, number and time of occurrence of impacts, as well as shape of the response spectra are in good agreement with experimental observations. Moreover, using the building pounding frame and the NSCD method, an estimation of a constant value for the coefficient of restitution was carried out. It is concluded that the NSCD method is a very numerically efficient tool in terms of reduction of CPU time and description of the impact physics. Consequently, this approach is amenable for fragility analysis of the dynamic response of structures involving a contact-impact phenomenon.

1. Introduction

Structural pounding during earthquakes is a recurrent phenomenon in dense urban settings; it occurs when the building separation is insufficient to accommodate the seismically induced displacements. For large earthquakes, the consequences of building pounding can be catastrophic (Fig. 1), as it was the case for the Mexico City earthquake of 1985, in which building pounding was the main cause of collapse in at least 15% of collapse observations (Bertero [1]; Rosenblueth and Meli [2]). A survey of the buildings damaged during the 1989 Loma Prieta earthquake (Kasai and Maison [3]) found that pounding occurred primarily in old multi-story masonry buildings, in most cases without separation; in contrast, pounding events were relatively minor in modern constructions. Similarly, structural pounding during the 2017 Puebla earthquake affected mostly very flexible flat-slab systems (Reinoso et al. [4]) built prior to 1985, which did not have the minimum separation required by the local seismic code.

Based on observations of the 1985 Mexico City earthquake and the 1989 Loma Prieta earthquake, Jeng et al. [7] identified the pounding categories summarized in Fig. 2. In each case, the pounding damage can range anywhere from minor architectural damage to partial or total collapse of the building. Indeed, the building pounding effects in Fig. 1a can be categorized as "mid-column pounding" or "pounding against a taller adjacent building". Likewise, the pounding category for the buildings in Fig. 1b is a good example of "torsional pounding" and "pounding with brittle facades". Karayannis et al. [8,9] studied the effects of pounding between reinforced concrete structures of different heights, including mid-column pounding, and torsional pounding. The study revealed the vulnerability and weaknesses of the different configurations, such as increased story shears and ductility demands at the contact floors. The aim of this study is on the numerical procedures to treat pounding, si ot is initially limited to study pounding between linear elastic structures of equal heights and co-planar slabs. However, future earthquake response studies will consider aspects such as pounding at intermediate story levels and pounding of torsionally coupled structures, which have been observed after earthquakes.

* Corresponding author.
E-mail address: thomas.langlade@insa-lyon.fr (T. Langlade).

https://doi.org/10.1016/j.engstruct.2021.112426
Received 10 November 2020; Received in revised form 24 March 2021; Accepted 19 April 2021

(a) Intermediate floor collapse (mid-story) of Hotel de Carlo in Mexico City, probably caused by pounding against the shorter building to the left; photograph taken after the Mw 8.1 Mexico earthquake [5]

(b) Pounding damage to the reinforced concrete frame and masonry infill building observed during the Mw 7.4, Izmit earthquake, Turkey, 1999 [6]

Fig. 1. Examples of building pounding damage during earthquakes. (See above-mentioned references for further information.)

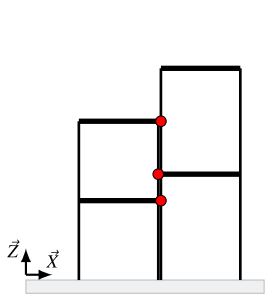

(a) Mid Column Pounding

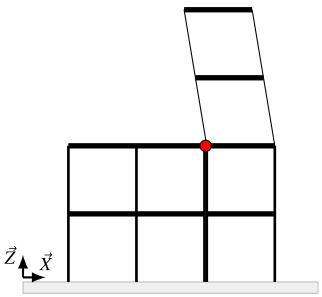

(b) Taller Adjacent Building

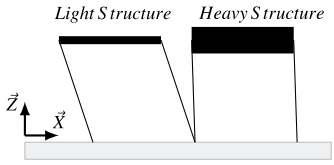

(c) Heavier Adjacent Building

(d) End Building Pounding

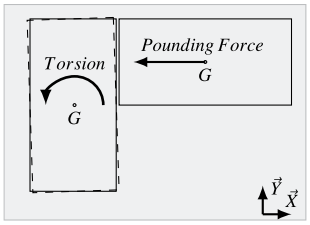

(e) Torsional Pounding

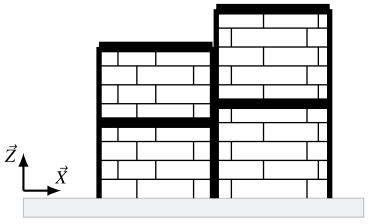

(f) Structures with superficial brittle facades

Fig. 2. Critical configurations of structures (Jeng et al. [7] and Cole et al. [31]).

In addition to an insufficient separation, building pounding occurs due to a combination of other factors (Bertero [10]), most commonly: (i) vague design guidelines and lack of engineering judgement; (ii) ground motion intensities higher than design values; (iii) inadequate structural configurations, particularly buildings with lateral-torsional coupling, soft stories, or low lateral stiffness and strength; and (iv) pre-existing tilt and ground deformations.

Separation guidelines in current seismic codes aim to avoid contact under maximum inelastic response of each adjacent structure. For instance, Eurocode 8 [11] and ASCE 7–16 [12] require that the maximum inelastic deformation of each building, referred to as δ_{M1} and δ_{M2}, "shall be determined at critical locations with consideration for translational and torsional displacements of the structures including torsional amplifications, where applicable", and that the net separation between the structures should be greater than $\sqrt{(\delta_{M1})^2 + (\delta_{M2})^2}$. Despite their simplicity and apparent conservatism (e.g., both structures reach simultaneously their maximum deformation in opposite directions), these rules do not guarantee a collision free response, mainly because of the large ground motion and building response uncertainties. Therefore, structural pounding in dense urban areas will probably continue occurring in future earthquakes.

Crozet [13] discusses several tests on building pounding (e.g., [15–19]) conducted on small scale structures, none of which are code-compliant. To our knowledge, existing studies about pounding on code-based buildings are mostly numerical or forensic. For instance, Favvata [14] studied pounding between an 8-story RC structure and a shorter much stiffer building, both designed according to the Eurocode 8 [11]. The study concludes that the Eurocode provisions for gap separation are somewhat conservative. Additionally, the study shows that large plastic deformations may develop in the building columns in the case of impact against slabs. Later, Karayannis et al. [9] showed that

Table 1
Main gap element formulations for dynamic pounding analysis.

Name	Impact Force $F(t)$	ξ_d	ξ_r
Hertz Non-Linear (HNL)[33,34]	$k_s\delta^{\frac{3}{2}}(t)$	/	/
HertzDamp Non-Linear (HDNL) [35]	$k_s\delta^{\frac{3}{2}}(t) + \xi_d\dot{\delta}(t)$	$k_s\left(\frac{8(1-e)}{5e(v_1^- - v_2^-)}\right)$	/
Linear Visco-Elastic (LVE) [18]	$k_s\delta(t) + \xi_d\dot{\delta}(t)$	$2\xi_r\sqrt{k_s\frac{m_1m_2}{m_1+m_2}}$	$\frac{\ln(e)}{\sqrt{\pi^2+(\ln(e))^2}}$
Modified Linear Visco-Elastic (MLVE) [24]	Approach period: $k_s\delta(t) + \xi_d\dot{\delta}(t)$ Restitution period: $k_s\delta(t)$		$\frac{1-e^2}{e(e(\pi-2)+2)}$
Non-Linear Visco-Elastic (NLVE) [21,25]	Approach period: $k_s\delta^{\frac{3}{2}}(t) + \xi_d\dot{\delta}(t)$ Restitution period: $k_s\delta^{\frac{3}{2}}(t)$	$2\xi_r\sqrt{k_s\sqrt{\delta}\frac{m_1m_2}{m_1+m_2}}$	$\frac{9\sqrt{5}}{2}\frac{1-e^2}{e(e(9\pi-16)+16)}$

torsional pounding between a moment frame building and a rigid shear wall building might result in increased story shears along the two principal axis of the moment frame building, and severe damage to its columns.

Elwardany et al. [15] concluded that infill panels may play a favourable role in preventing pounding, at the expense of increasing locally the building stiffness. Like Favvata et al. [16], they warned against the tall first story height and especially the pilotis type building configuration (open columns with no infills at the ground level), where pounding at an upper floor could significantly increase localized drift and shear demand. Regular distributed panels would not eliminate the risk, but at least reduce the frequency of these mechanisms. Also, Karayannis et al. [17] studied the effect of pounding on structures with infill and their effects on the external joints, either considered rigid, or modelled with a rotational spring element. The authors concluded that the exterior joints develop plastic hinges, with an undesirable increase of the interstory-drifts ranging from 34% to 64%. These studies support the Anagnostopoulos [18] assertion that pounding has negative effects, both on elastic and inelastic structures.

Overall, numerical models of code-designed buildings confirm the negative effect of collision on the structural capacity and engineering parameters of interest, both for elastic as well as inelastic buildings.

Modelling the seismic response of adjacent buildings subject to pounding remains a very challenging problem, mainly because of the large number of parameters involved and the coarse assumptions typically made to account for the energy transfer between buildings. However, the use of simplified models allows reproducing the key response parameters of the system under different loading conditions. Two modelling approaches for pounding exist in the literature, commonly referred to as the Penalty Method (PM) (Anagnostopoulos[18–20], Jankowski [21–24], Naderpour et al.[25], Xu et al. [26]) and the Lagrange Multipliers Method (LMM) (Papadrakakis and Mouzakis [27,28], Cole [29], Ambiel et al. [30]).

In the former PM approach, the contact forces are modelled through a physical compression gap element between each pair of contact points. Because of its simplicity, the PM approach is widely used in structural engineering and is readily available in most finite element software in the form of one-dimensional nonlinear gap elements. These gap elements allow transferring energy between the two structures and account for local energy dissipation; their main drawback, however, is that the computation of contact forces relies on semi empirical (often non-physical) coefficients, which require experimental validation (Candia et al. [32]). For instance, one of the simplest gap element formulations is the Linear Visco-Elastic (LVE) model, where the contact force between two nodes during a collision is given by Eq. 1. Similar gap element formulations are summarized in Table 1.

$$F(t) = k_s\delta(t) + \xi_d\dot{\delta}(t) \tag{1}$$

where δ(t) is the interpenetration depth (i.e., the amount of overlap between the colliding nodes); $\dot{\delta}$(t) the interpenetration rate; and k_s and ξ_d are the empirical coefficients representative of the stiffness and damping of the contact interface, respectively. While the stiffness parameter k_s controls the amount of interpenetration of a contact pair, the damping coefficient ξ_d controls the amount of energy dissipated during that contact. Several formulations have been proposed to express ξ_d as a function of the coefficient of restitution e (Table 1), defined as the ratio between the relative velocities of two particles or bodies after and before impact. The parameter e takes values between 0 and 1, where $e = 0$ represents a perfectly inelastic impact, and $e = 1$ represents a perfectly elastic impact with no energy loss.

m_1 and m_2 are nodal masses; e is the coefficient of restitution; ξ_d and ξ_r are respectively the damping coefficient and damping ratio. Approach period means means that $\dot{\delta} > 0$, when relative velocity is positive, thus interpenetration is ongoing. Restitution period means that $\dot{\delta} \leqslant 0$, when relative velocity is negative, thus when bodies are departing from each other.

Several authors (Jankowski [22,24], Khatami [36], Xu [26], Crozet [37]) have studied the influence of the gap element parameters and the dynamic response of colliding bodies. For instance, Crozet et al. [38] found that the contact stiffness should be greater than ten times the stiffness of the most rigid impacting body, and that the maximum time step for a dynamic analysis should be limited to one-fourth of the smallest vibration periods of the two buildings. These simple rules allow minimizing the contact duration, preserve the system kinematics, and yield acceptable results and computational runtimes. Studying the response of single degree of freedom (SDOF) systems, Anagnostopoulos [18] found that the contact stiffness has a large effect on the SDOFs accelerations and forces, but a marginal effect on their displacements. Later, based on experimental evidence, Khatiwada et al. [39] concludes that the contact stiffness derived from small scale specimens cannot be applied to prototype scale buildings. The author acknowledges the PM limitations regarding the sensitivity of the building response to the value of the stiffness parameter k_s. The contact force $F(t)$ also depends on the damping parameter ξ_d, which accounts for the energy dissipation during contact (e.g., Table 1). While Anagnostopoulos [18] showed that ξ_d has a marginal influence on the building response, Khatiwada et al. [39] showed that the displacement history of colliding SDOF does depend on ξ_d for certain high values of k_s.

In the Lagrange Multipliers Method (LMM), which derives from the principle of conservation of linear momentum, the contact kinematics is enforced through external loads, and the energy dissipated during inelastic collisions is accounted for by using either the kinematics and internal equilibrium of the system [30,27,40], or the coefficient of restitution e (Acary [41]). These external loads enforce a "strict no-penetration condition", but they introduce an instantaneous change in the particle velocities, excite high frequency modes, and create large spurious internal forces.

Reported applications of the PM to building pounding problems are significantly larger than LMM applications, in part, because the implementation of LMM solutions is cumbersome, also with respect to

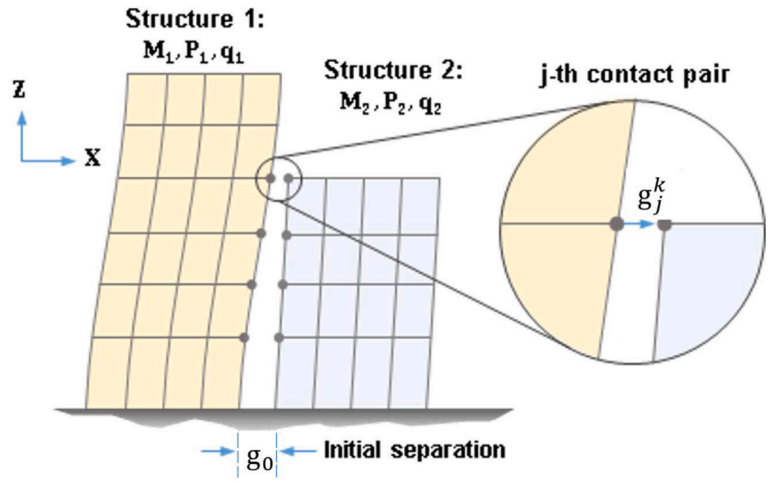

Fig. 3. Idealized structures with coplanar diaphragms in deformed configuration; solid circles represent the contact pairs along the contact interface.

convergence and stability. However, the use of LMM is appealing if the coefficient of restitution e is used since it has a simpler physical interpretation. Therefore, the goal of this article is to present a complementarity method based solution for structural pounding during earthquakes (it has a similar formulation than the LMM); this solution overcomes some of the difficulties found in current LMM implementations, and is based on a single empirical parameter, which simplifies the model definitions.

Indeed, the structural pounding model is based on the Non-Smooth Contact Dynamics (NSCD) algorithm developed by Moreau [42] and extended by Jean [43] and Acary [40,41,44,45] to account for deformable systems. To our knowledge, the use of the NSCD approach to structural pounding problems has not been reported in the literature. In the following sections, the formulation of the NSCD algorithm is presented along with two validation examples: (i) the "bouncing ball test"; and (ii) a plane frame pounding tests, where the NSCD approach is used to reproduce the shaking table response of one and two-story buildings.

2. NSCD method

This section presents the NSCD approach and integration scheme illustrated by the case of two collision-prone linear multi degree of freedom (MDOF) systems as schematically shown by Fig. 3. Although only coplanar diaphragms are shown in this figure in which contacts occur at story levels, the formulation presented is applicable to an arbitrary distribution of collision points such as column-diaphragm impacts. However, for simplicity in the presentation we consider here two planar moment resisting frames with lumped masses and net separation g_0. Each structure is characterized by a constant mass matrix $\mathbf{M}_i$, and a vector of nonlinear internal forces $\mathbf{P}_i(\mathbf{q}_i, \dot{\mathbf{q}}_i)$ defined in generalized coordinates $\mathbf{q}_i$,with $i = 1, 2$. Pounding forces may develop at n discrete locations along the contact interface (i.e., node-to-node contact) between pairs of point-masses on each building, henceforth a contact pair. The impact and energy dissipation on each contact pair are modelled using Newton's impact law and the conservation of linear momentum.

The equations of motion for both systems can be written in augmented form as

$$\mathbf{M}\ddot{\mathbf{q}} + \mathbf{P}(\mathbf{q}, \dot{\mathbf{q}}) - \mathbf{F} = \mathbf{0} \tag{2}$$

where $\mathbf{q} = [\mathbf{q}_1^T \mathbf{q}_2^T]^T$, $\dot{\mathbf{q}}$ and $\ddot{\mathbf{q}}$ the are the first and second time derivatives of $\mathbf{q}$, respectively. The term $\mathbf{P}(\mathbf{q}, \dot{\mathbf{q}}) = [\mathbf{P}_1^T \mathbf{P}_2^T]^T$ is the vector of internal forces, and the composite mass matrix $\mathbf{M}$ is the block-diagonal concatenation of matrices $\mathbf{M}_1$ and $\mathbf{M}_2$. $\mathbf{F}$ is a set of external forces conjugated in work with $\mathbf{q}$, which accounts for static and dynamic loads.

The NSCD integration scheme [43], presented herein, is used to solve Eq. 2 in discrete time. The method uses the Moreau-Jean [42] stepping algorithm to step from time t_i to $t_{i+1} = t_i + \Delta t$ in addition to the Signorini-Moreau conditions for contact detection. The contribution of Acary [45] allowed for the application of the method to deformable bodies, and highlighted its energy conservation properties [44].

2.1. Moreau-Jean stepping algorithm

After integrating Eq. 2 from t_i to t_{i+1} and approximating the integral of the nonlinear forces with the midpoint rule, the equation of motion can be written in incremental form as presented in Eq. (4), where $\mathbf{R}_{k+1}$ stands for the residuals at time t_{i+1},$\mathbf{G}_i = \int_{t_i}^{t_{i+1}} \mathbf{F} dt$, and the sub-index $i+\theta$ denotes the time $t_{i+\theta} = t_i + \theta\Delta t$.

$$\int_{t_i}^{t_{i+1}} \mathbf{M}\ddot{\mathbf{q}} dt + \int_{t_i}^{t_{i+1}} \mathbf{P} dt - \int_{t_i}^{t_{i+1}} \mathbf{F} dt = \mathbf{0} \tag{3}$$

$$\mathbf{R}_{k+1} = \mathbf{M}(\dot{\mathbf{q}}_{i+1} - \dot{\mathbf{q}}_i) + \mathbf{P}_{i+\theta}\Delta t - \mathbf{G}_i = \mathbf{0} \tag{4}$$

Expressions for $\mathbf{q}_{i+1}, \dot{\mathbf{q}}_{i+\theta}$, and $\mathbf{q}_{i+\theta}$ are shown in Eqs. (5)–(7) based on the Euler-θ approximation method.

$$\mathbf{q}_{i+1} = \mathbf{q}_i + \dot{\mathbf{q}}_{i+\theta}\Delta t \tag{5}$$

$$\mathbf{q}_{i+\theta} = (1-\theta)\mathbf{q}_i + \theta\mathbf{q}_{i+1} \tag{6}$$

$$\dot{\mathbf{q}}_{i+\theta} = (1-\theta)\dot{\mathbf{q}}_i + \theta\dot{\mathbf{q}}_{i+1} \tag{7}$$

The Moreau-Jean algorithm embedded in the NSCD approach uses $\theta = \frac{1}{2}$, which results in an implicit integration scheme unconditionally stable relative to Δt, similar to the algorithms by Euler and Newmark. If no collisions occur between t_i and t_{i+1}, the velocities $\dot{\mathbf{q}}_{i+1}$ can be obtained solving Eq. (4) (i.e., $\|\mathbf{R}_{k+1}\| \leqslant \epsilon$, where ϵ is a scalar arbitrarily taken close to 0) using the Newton Raphson (NR) algorithm, in which case the velocities in the $(k+1)th$ NR iteration can be written as

$$\dot{\mathbf{q}}_{i+1}^{k+1} = \dot{\mathbf{q}}_{i+1}^{k} - \left(\mathbf{J}^k\right)^{-1} \mathbf{R}_{i+1}^{k} \tag{8}$$

where the Jacobian $\mathbf{J}^k = \frac{\partial \mathbf{R}_{i+1}^k}{\partial \dot{\mathbf{q}}_{i+1}^k}$ is defined in terms of the tangent damping and stiffness operators $\mathbf{C}_{i+\theta}^{t,k}$ and $\mathbf{K}_{i+\theta}^{t,k}$, respectively, as

$$\mathbf{J}^k = \mathbf{M} + \mathbf{C}_{i+\theta}^{t,k}\Delta t\,\theta + \mathbf{K}_{i+\theta}^{t,k}\Delta t^2\theta^2 \tag{9}$$

2.2. Contact detection and impact forces

If the relative displacements between the buildings are sufficient to close the gap, a collision takes place and a set of impact forces must be

Table 2
NSCD method algorithm.

(i) For the *i-th* iteration
- $k = 1$
- $\mathbf{p}_{i+1}^{k} = \mathbf{0}$
- $\dot{\mathbf{q}}_{i+1}^{k} = \dot{\mathbf{q}}_i$
- $\dot{\mathbf{g}}_{i+1}^{k} = \dot{\mathbf{g}}_i = \mathbf{H}\dot{\mathbf{q}}_i$
- Eq. (13) DOF contact prediction: $\widehat{\mathbf{g}}_{i+1} = \mathbf{g}_i + \gamma \Delta t \dot{\mathbf{g}}_i$
- Find Ω such as $\widehat{\mathbf{g}}_{i+1,\Omega} \leqslant 0$

(ii) Kinematic first estimation from *Euler* implicit + θ method
- Eq. (7) $\dot{\mathbf{q}}_{i+\theta}^{k} = (1-\theta)\dot{\mathbf{q}}_i + \theta \dot{\mathbf{q}}_{i+1}^{k}$
- Eq. (5) $\mathbf{q}_{i+1}^{k} = \mathbf{q}_i + \dot{\mathbf{q}}_{i+\theta}^{k} \Delta t$
- Eq. (6) $\mathbf{q}_{i+\theta}^{k} = (1-\theta)\mathbf{q}_i + \theta \mathbf{q}_{i+1}^{k}$

(iii) Assembling of $\mathbf{J}^k$, $\widehat{\mathbf{R}}^k$ and $\mathbf{R}_c^k$
- Eq. (9) $\mathbf{J}^k = \mathbf{M} + \mathbf{C}_{i+\theta}^{t,k}\theta\Delta t + \mathbf{K}_{i+\theta}^{t,k}\theta^2\Delta t^2$
- Eq. (4) $\mathbf{R}^k = -\mathbf{M}\left(\dot{\mathbf{q}}^k - \dot{\mathbf{q}}_i\right) - \left[\mathbf{C}_{i+\theta}^{t,k}\dot{\mathbf{q}}_{i+\theta}^{k} + \mathbf{K}_{i+\theta}^{t,k}\mathbf{q}_{i+\theta}^{k}\right]\Delta t - \mathbf{G}_i$
- Eq. (14) $\widehat{\mathbf{R}}^k = \mathbf{M}(\dot{\mathbf{q}}_{i+1} - \dot{\mathbf{q}}_i) + \mathbf{P}_{i+\theta}\Delta t - \mathbf{G}_i - \mathbf{H}^T\mathbf{p}_{i+1}$
- $\mathbf{R}_c^k = 1$ to force the entry in the Solving Algorithm

(iv) Beginning of a Solving Algorithm to annihilate $\left\|\widehat{\mathbf{R}}^k\right\|$ and $\left\|\mathbf{R}_c^k\right\|$
- While $\left\|\widehat{\mathbf{R}}^k\right\| > \epsilon$ and $\left\|\mathbf{R}_c^k\right\| > \epsilon_c$

(v) Solving operators
- $\dot{\mathbf{g}}_{i+1}^{k} = \mathbf{H}\dot{\mathbf{q}}_{i+1}^{k}$
- Eq. (19) $\mathbf{b}^k = \mathbf{H}(\mathbf{J}^k)^{-1}\mathbf{R}^k + \dot{\mathbf{g}}_{i+1}^{k}$
- Eq. (20) $\mathbf{W}^k = \mathbf{H}(\mathbf{J}^k)^{-1}\mathbf{H}^T$

(vi) Calculation of $\mathbf{p}_{i+1}^{k}$, (Eqs. (17, 18))
- For $\alpha \in \Omega$
  - $\dot{\mathbf{g}}_\alpha = -e\mathbf{H}\dot{\mathbf{q}}_{i,\alpha}$
  - $\mathbf{p}_{i+1,\alpha}^{k} = max\left[0, \frac{1}{\mathbf{W}_{\alpha,\alpha}^{k}}\left(-\mathbf{b}_\alpha^k + \dot{\mathbf{g}}_\alpha - \sum_{\beta\neq\alpha}\mathbf{W}_{\alpha\beta}^{k}\mathbf{p}_{i+1}^{k} + \mathbf{W}_{\alpha\alpha}^{k}\mathbf{p}_{i+1,\alpha}^{k}\right)\right]$
- End For Loop

(vii) New $\dot{\mathbf{q}}^k$ determination
- Eq. (14) $\widehat{\mathbf{R}}^k = \mathbf{R}^k + \mathbf{H}^T\mathbf{p}_{i+1}^{k}$
- Eq. (8) $\dot{\mathbf{q}}_{i+1}^{k+1} = \dot{\mathbf{q}}_{i+1}^{k} - (\mathbf{J}^k)^{-1}\widehat{\mathbf{R}}^k$

(viii) Kinematic update as in (ii), (Eqs. (7, 5,6))

(ix) Update of $\mathbf{C}_{i+\theta}^{t,k}, \mathbf{K}_{i+\theta}^{t,k}, \mathbf{J}^k$ (Eq. (9)) and $\widehat{\mathbf{R}}^k$, (Eq. (4))

(x) Update of $\mathbf{R}_c^k$ (Eq. (21))
- $\mathbf{R}_c^k = \mathbf{p}_{i+1,\Omega}^{k} - max\left(0, \mathbf{p}_{i+1,\Omega}^{k} - \rho(\mathbf{W}_{(\Omega,\Omega)}\mathbf{p}_{i+1,\Omega}^{k} + \mathbf{b}_\Omega + e\dot{\mathbf{g}}_{i,\Omega})\right)$
- $k = k + 1$

End While Loop
- $\dot{\mathbf{q}}_i = \dot{\mathbf{q}}_{i+1}^{k+1}$

End For Loop

added to enforce the no-penetration condition. The separation $\mathbf{g}_i$ and separation rate $\dot{\mathbf{g}}_i$ at the n contact pairs is obtained from the linear relation

$$\mathbf{g}_i = \mathbf{H}\mathbf{q}_i + \mathbf{g}_0 \tag{10}$$

$$\dot{\mathbf{g}}_i = \mathbf{H}\dot{\mathbf{q}}_i \tag{11}$$

where $\mathbf{H}$ is a kinematic transformation matrix, and $\mathbf{g}_0 = [g_0^1 g_0^2 \cdots g_0^n]^T$ is the initial separation along the contact interface, as shown in Fig. 3. When stepping from t_i to t_{i+1}, pounding will occur if the predicted gap at time t_{i+1} is less than zero at any of the contact nodes, as shown in Eq. 12. In the current NSCD approach, the Signorini-Moreau contact condition is used to predict the separation at time t_{i+1} as a function of the separation rate shown in Eq. 13, where the constant γ takes a value of 3/2.

$$\widehat{\mathbf{g}}_{i+1} \leqslant 0 \tag{12}$$

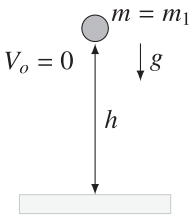

Fig. 4. Bouncing ball test case.

$$\widehat{\mathbf{g}}_{i+1} = \mathbf{g}_i + \gamma\Delta\dot{\mathbf{g}}_i \tag{13}$$

Let us denote Ω as the set of all contact pairs that satisfy Eq. (12), and α an arbitrary contact pair that belongs to the Ω set. The kinematic condition on the rate of separation based on Newton's impact law can be stated as: $\dot{\mathbf{g}}_{i+1,\alpha} = -e\dot{\mathbf{g}}_{i,\alpha}$, where e is the coefficient of restitution. To compute the new velocities and enforce the contact kinematics, an impulse vector $\mathbf{p}_{i+1}$ is added to the equilibrium Eq. (4) in addition to the linear constraints in Eqs. (15) and (16).

$$\widehat{\mathbf{R}}_{k+1} = \mathbf{M}\left(\dot{\mathbf{q}}_{i+1} - \dot{\mathbf{q}}_i\right) + \mathbf{P}_{i+\theta}\Delta t - \mathbf{G}_i - \mathbf{H}^T\mathbf{p}_{i+1} = \mathbf{0} \tag{14}$$

$$\dot{\mathbf{g}}_{i+1} \leqslant -e\dot{\mathbf{g}}_i \tag{15}$$

$$\mathbf{p}_{i+1} \geqslant \mathbf{0} \tag{16}$$

Solving the system's unknowns $\dot{\mathbf{q}}_{i+1}$ and $\mathbf{p}_{i+1}$ from Eqs. (14)–(16) is equivalent to solving a linear optimization problem, for which a vast body of literature exists. Herein, we propose the Gauss–Seidel type solution introduced by Acary [45], which uses a successive elimination of equations. Thus, the impulse at the α-th contact pair within the k-th NR iteration is computed as

$$\mathbf{p}_{i+1,\alpha}^{k} = \frac{1}{\mathbf{W}_{\alpha,\alpha}^{k}}\left(-\mathbf{b}_\alpha^k + \dot{\mathbf{g}}_\alpha - \sum_{\beta\neq\alpha}\mathbf{W}_{\alpha\beta}^{k}\mathbf{p}_{i+1}^{k} + \mathbf{W}_{\alpha\alpha}^{k}\mathbf{p}_{i+1,\alpha}^{k}\right) \geqslant \mathbf{0} \tag{17}$$

$$\dot{\mathbf{g}}_\alpha = -e\mathbf{H}\dot{\mathbf{q}}_{i,\alpha} \tag{18}$$

The terms b_α^k and $W_{\alpha\beta}^{k}$, respectively, the α-entry and (α,β) entries of matrices $\mathbf{b}^k$ and $\mathbf{W}^k$ defined as

$$\mathbf{b}^k = \mathbf{H}\left(\mathbf{J}^k\right)^{-1}\mathbf{R}^k + \mathbf{H}\dot{\mathbf{q}}_{i+1}^{k} \tag{19}$$

$$\mathbf{W}^k = \mathbf{H}\left(\mathbf{J}^k\right)^{-1}\mathbf{H}^T \tag{20}$$

A residue on the impact force to ensure the validation of the impulse is introduced with the following formulation proposed by Acary in collaboration with the authors, with ρ a scalar superior or equal to 1.

$$\mathbf{R}_c^k = \mathbf{p}_{i+1,\Omega_\alpha}^{k} - max\left(0, \mathbf{p}_{i+1,\Omega_\alpha}^{k} - \rho\left(\mathbf{W}_{(\Omega_\alpha,\Omega_\alpha)}\mathbf{p}_{i+1,\Omega_\alpha}^{k} + \mathbf{b}_{\Omega_\alpha} + e\dot{\mathbf{g}}_{i,\Omega_\alpha}\right)\right) \tag{21}$$

It must be pointed out that the entire NSCD method is independent of the acceleration, which is undefined due to the instantaneous change of velocities induced by Newton's law. Thus, the acceleration at each time-step is obtained with the fundamental theorem of calculus, but its resulting value depends on the time-step chosen.

The algorithm of the NSCD method is presented in Table 2.

3. Bouncing Ball test

The capabilities of the NSCD and PM approaches are compared for a test case of a rigid ball bouncing on a rigid floor (Fig. 4). The analytical solution is known from Acary [41], so the parameters used are the same. The ball has a mass $m_1 = 1$ kg and is released from a height $h = 1$ m, with a zero initial velocity V_o and vertical acceleration $g = 2\ m/s^2$.

The LVE and NLVE (Jankowski[22]) PM models are tested. A

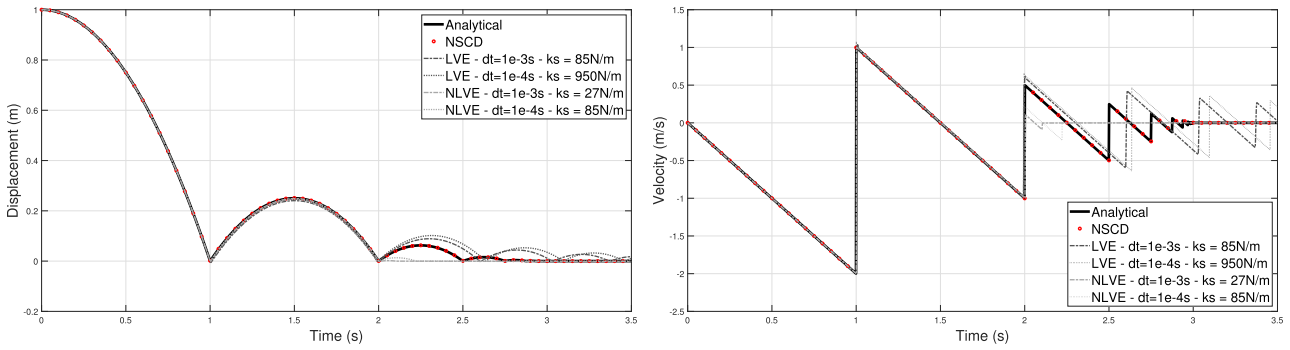

(a) Bouncing ball - Displacements (b) Bouncing ball - Velocities

Fig. 5. Comparison of the NSCD and PM results for the bouncing ball test case.

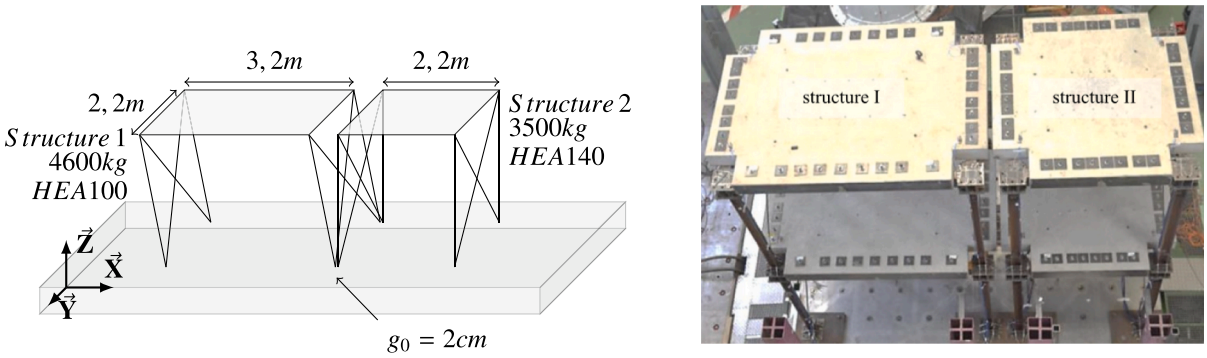

(a) Scheme of the single-story structures (b) Two-story structures[26]

Fig. 6. Single-story and Two-story Structures.

sensitivity analysis is performed to assess the value of the contact stiffnesses k_s delivering the best results. The mass ratio $\frac{m_1 m_2}{m_1+m_2}$ in Table 1 simplified to m_1. Two time steps are chosen, 10^{-3}s and 10^{-4}s, to highlight the dependency of the results accuracy on time step, and the study length is fixed to 3.5s. The coefficient of restitution e equals to 0.5. Figs. 5a and b present respectively the displacements and velocities of the three approaches, analytical (black curve), NSCD (red dots), and PM (LVE and NLVE in grey curves).

It is apparent that the NSCD procedure provides the exact response without the need of defining a contact stiffness and no time step to refine. As opposed to the NSCD method, it is highly difficult to reproduce the analytical kinematics with the PM after the second rebound. The out-of-phase motion spotted for $\Delta t = 10^{-3}s$ is barely improved by refining it to $10^{-4}s$, and at to the cost of increasing computation time. Also, the impact stiffness yielding the best results changes with time step and the impact law considered. This comparison of both methods is now to be applied in the frame of a scale 1:1 building pounding system.

4. Plain Frame Pounding test

4.1. Shaking table experimental set-up

In the frame of the ANR SINAPS[1] project to improve knowledge on vulnerability and resistance of strategic buildings (e.g., nuclear power plants) against earthquakes, series of pull back and seismic tries to induce pounding between single-story or two-story structures were carried out at the Commissariat à l'Energie Atomique et aux Energies Alternatives (CEA) de Saclay by Crozet et *al.* [13,37,38].

The two steel-framed structures with rectangular reinforced concrete slabs were fixed side by side to the shaking table AZALEE of the EMSI laboratory[2]. These structures are identified respectively 1 and 2 from left to right (Fig. 6b, they can alternatively be set up as one story high (2.5 m), or two stories high (5 m) by adding or removing additional elements. The gap separation is also adjustable. Finally, to keep the structural motion only in the longitudinal axis, bracing systems (steel cables) are used to limit transverse and torsional displacements (Figs. 6a and b).

To ensure impact occurrences under seismic motion, the modal responses of both structures are different (Table 7). Thus, one structure is heavier (9200 kg versus 7000 kg), while the other one is stiffer (HEA140 versus HEA100 steel columns). Sensors are installed on the shaking table, slabs and columns to measure the accelerations with low frequency capacitive accelerometers (0–150 Hz) and high-frequency piezoelectric accelerometers (0–4000 Hz). A low-pass filter with a cut-off frequency of 2000 Hz was applied by Crozet et al. [13] to the input ground motions to prevent any aliasing effect and prevent from spurious high-frequency content in the numerical comparison.

Four ground motions were used to excite both single-story and two-story structures, Cadarache (artificial acceleration), El Centro (1940), Northridge (1994) and Kobe (1995). Different amplification factors were applied to generate from these ground motions different Peak Ground Accelerations (PGA) ranging from 0,1 g to 0,45 g, with g the acceleration of gravity.

[1] ANR, Agence Nationale de la Recherche, SINAPS, Séisme et Installations Nucléaires, Améliorer et Pérenniser la Sûreté - https://www.institut-seism.fr/projets/sinaps/.

[2] EMSI Laboratory, Laboratoire d'Etudes de Mécanique SIsmique - http://www-tamaris.cea.fr/index.php.

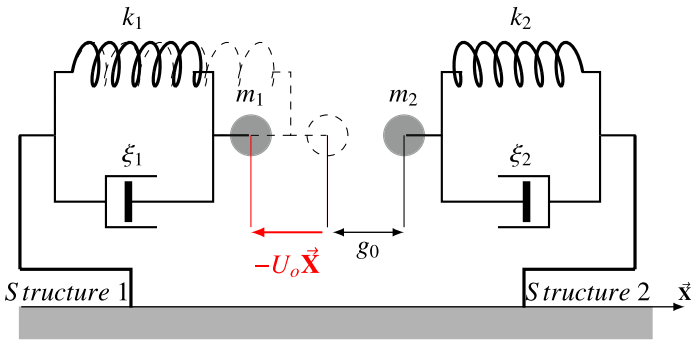

Fig. 7. Pull back test SDOF model.

Table 3
Structural model data.

Data	Structure 1	Structure 2
Fundamental Frequency (Hz)	3.50	6.55
Fundamental Period (s)	0.29	0.15
Mass (kg), m_i	4600	3500
Structure Stiffness (N/m), k_i	2.11e6	5.31e6
Damping Coefficient (%), ξ_i	0.4 to 0.6	0.4 to 0.6

Table 4
NSCD and PM parameters.

Models	k_s (N/m)	ξ_d (%)	ξ_r (%)	e
NSCD method	/	/	/	[0.2;0.6;0.9]
Anagnostopoulos [18]**	[0.01;0.1;1;10;100] $\max(k_1,k_2)$	8.46e4	0.136	0.65
Jankowski [23]***		*	0.373	
Khatami et al. [36]****		*	0.0428	

** The formulation $\xi_d = 2\xi_r\sqrt{k_s\sqrt{\delta}\,\dfrac{m_1 m_2}{m_1+m_2}}$ with δ the interpenetration distance.
*** With ξ_r and ξ_d expressed in (LVE) in Table 1.
**** With ξ_r and ξ_d expressed as in (NLVE) in Table 1.
***** With $\xi_r = \dfrac{(1-e)e^{0.204}}{e^{\alpha+0.204}+3.351e\pi}$ and $\alpha = 1.05e^{0.653}$.

4.2. Validation of model parameters: Pull back tests

This subsection focuses on determining a value of the coefficient of restitution e from experimental pull back tests. It also compares results from the NSCD method and PM in a real scale pounding system. Indeed, no consensual formulation has been delivered in the literature to calculate e before collision, and in most cases its value is defined constant and arbitrary between 0 and 1. Jankowski [24,46] worked on assessing the variation of e with the relative velocities by dropping balls on rigid floors made of different materials. However, Crozet [13], despite confirming the trend of Jankowski curves, pointed out the high difficulty to experimentally assess such value with monitored real scale structures. Thus, constant values of e are assumed in this article.

The pull back tests are done in four steps and only applied to the single-story structures whose slabs are separated by a 2 cm average distance S. First, Structure 1 is fixed to a reference frame by electric suction pads. Secondly, the shaking table is slowly moved longitudinally 2 cm to 4 cm apart, deforming the columns of Structure 1. The third step is a symmetry check, to verify that the pads each take the same load. Finally, the suction pads power supply is cut off, the left structure is released and is allowed to impact the right-hand side structure. The scheme to illustrate the set-up and data is shown in Figs. 6a and 7.

In Fig. 7, m_j, ξ_j and k_j are respectively the mass, damping coefficient, and stiffness of the SDOF j, with $j = [1;2]$. g_0 is the separation distance between structures, and U_o is the pull back distance of the left-hand side structure before its release.

The Linear Visco-Elastic (LVE) model is used herein following the Anagnostopoulos [18] approach, as well as the Non-Linear Visco-Elastic models (NLVE) by Jankowski [23] and Khatami [36]; e is fixed at 0.65. Regarding the contact stiffness, it is calibrated in a range centred around the maximum value of k_1 and k_2, corresponding to the stiffness along the longitudinal axis of structures 1 and 2, respectively. For the NSCD method, results are analysed for values of e equal to 0.2, 0.6 and 0.9; the time step equals 10^{-3}s. Tables 3 and 4 present the available data and the analytical parameters of the impact models of the structures. Results of

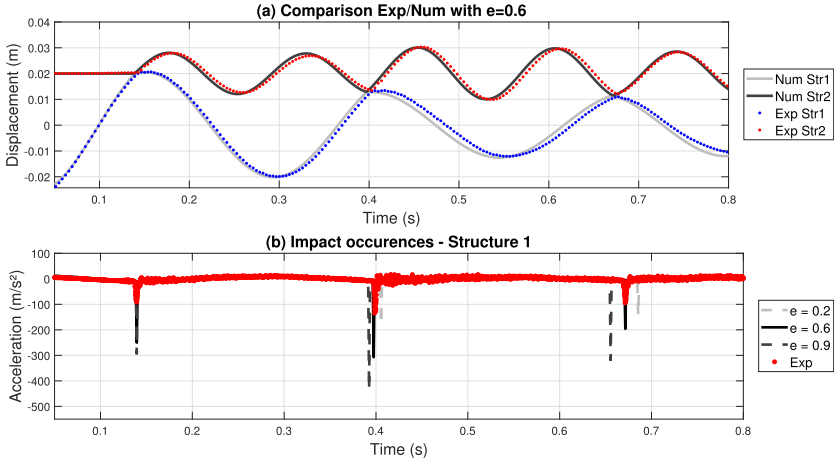

Fig. 8. NSCD method: evaluation of e.

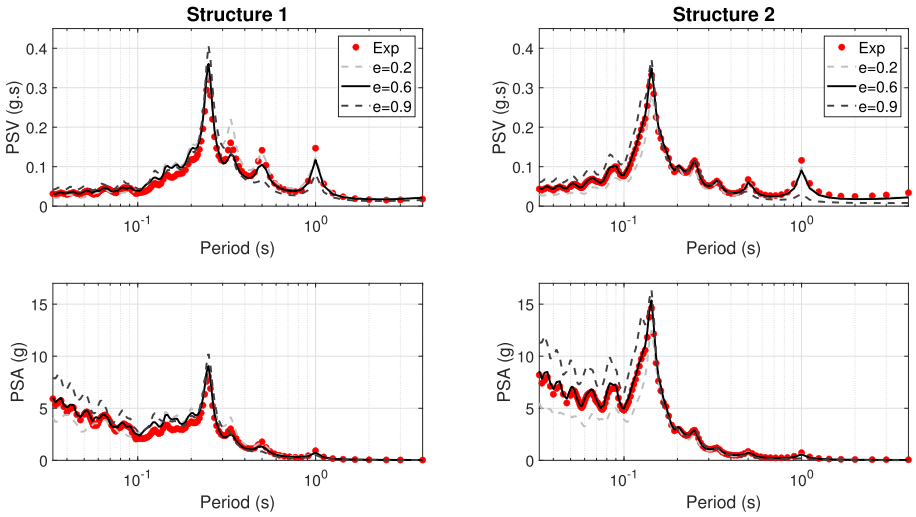

Fig. 9. Pull back test: 5% damped PSV and PSA spectra for different values of e.

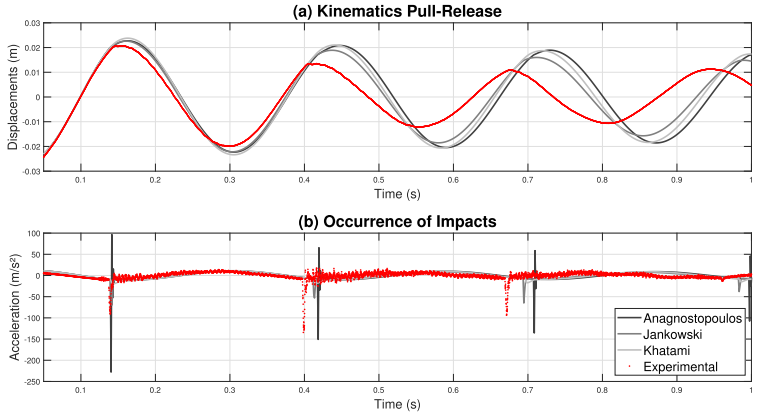

Fig. 10. Comparison of PM with experimental values: $k_s = 0.01max(k_1, k_2), \Delta t = 10^{-3}s$.

the analytical models are then compared with the experimental outcomes.

Since the transverse and torsional eigenfrequencies of the single-story structures were not available, the finite elements models used for the pull back and seismic tests are respectively SDOF and planar-frame models. They fit the experimental modal and damping behaviour, as observed graphically in Fig. 8 and more thoroughly explained in Section 4.3.

NSCD results: Sixteen pull back tests were performed [13], pulling distances ranged from 2.1 cm to 3.4 cm, and six of them were modelled numerically. Different e values of 0.2, 0.6 and 0.9 were investigated. Fig. 8a shows, for a pull back test of 2.4 cm, the displacements of the two contact degrees of freedom compared with the experimental ones for an e value of 0.6.

The building response measured and computed in the pull back tests, Fig. 8a, are in good agreement, in terms of the instants of impact occurrence, the displacement and acceleration histories, as well as the energy loss and damping. A similar quality of results was observed in the

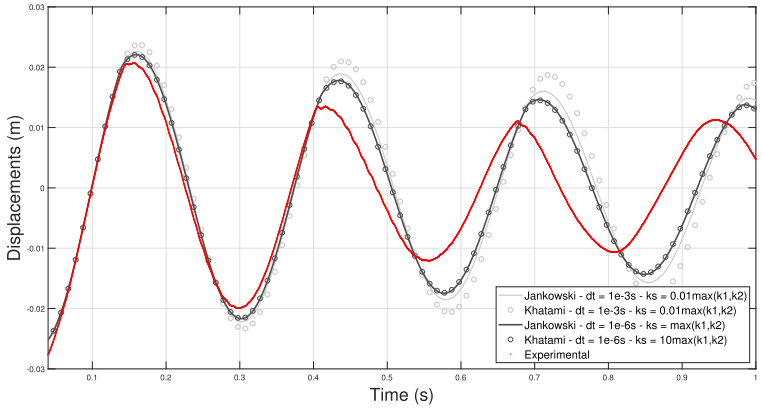

Fig. 11. Structure 1: Effects of Δt and k_s on results accuracy.

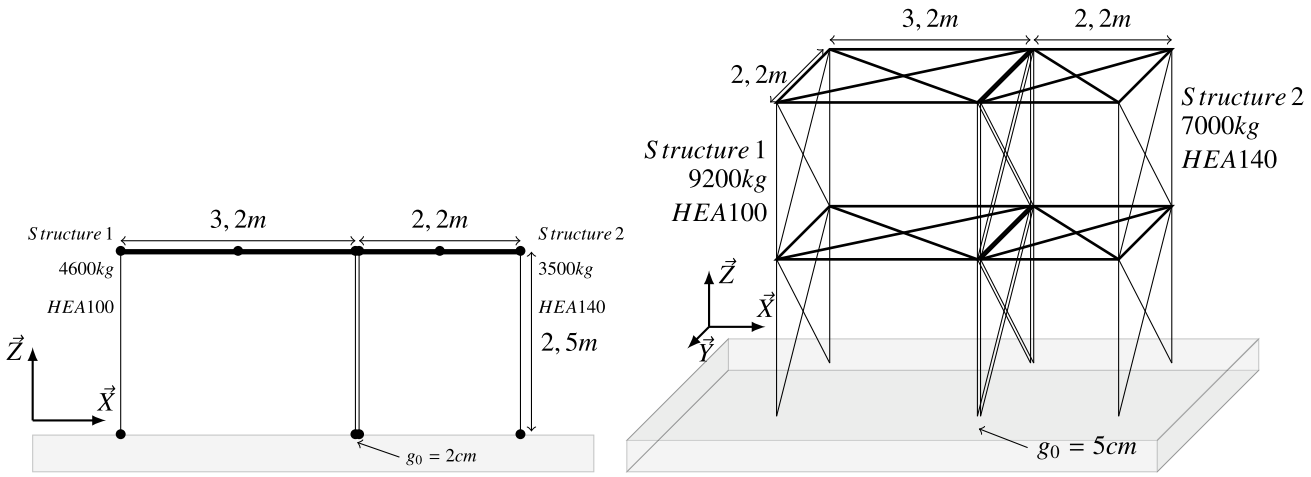

(a) Single-story 2D-Frame model (b) Two-story 3D-Frame model

Fig. 12. Numerical models used for seismic tests.

five remaining pull back tests. Stiffness and damping parameters inferred from these tests were used in the subsequent simulations presented hereafter. Fig. 8b shows the measured acceleration history in Structure 1 and the computed response for three values of the coefficient of restitution, $e = 0.2$, 0.6 and 0.9. In this figure the marked acceleration peaks are a result of structural pounding; despite some differences in the acceleration amplitude (resulting from the fundamental theorem of calculus, cf. end of Section 2), it is apparent that the value $e = 0.6$ results on perfectly synchronized pounding occurrences relative to the measured response.

Fig. 9 presents the 5% damped pseudo-velocity (PSV) and pseudo-acceleration (PSA) spectra of Structure 1 (left figure) and 2 (right figure) generated with different values of e. They are compared to the experimental averaged pseudo-accelerations. Matching is excellent with $e = 0.6$ for both structures in the full range of periods. However, differences in amplitude appear for $e = 0.2$ and 0.9 in the lower periods where both curves depart from the experimental one.

PM results: to improve legibility, only the Structure 1 responses are presented in Fig. 10. For $\Delta t = 10^{-3}$s, the contact stiffness equal to $0.01max(k_1, k_2)$ yields the best results for each model, but out-of-phase motion increases at each impact. The amplitudes and impact occurrences are afterwards less and less accurate. Taking a higher stiffness (10 times the highest value of contact stiffness, by Anagnostopoulos [18]), would decrease the phase shift. Nevertheless, it also brings non-realistic kinematic values, unless one takes a much smaller time step and thus increasing the computation cost.

Fig. 11 presents the displacements with both 10^{-3}s and 10^{-6}s time steps for Jankowski [23] and Khatami [36] models. Similar to the bouncing ball case, the contact stiffness may vary as much as two or three orders of magnitude if the time step is reduced by a factor of 1000. Even though the accuracy of the response is not improved significantly, the computation time is also increased by a 1000 times, which may be unjustified.

The value $e = 0.6$ in the NSCD method is assumed in all future calculations involving reinforced concrete coplanar diaphragms. On this particular study case, the NSCD method has proven its accuracy and ergonomics capabilities into yielding outcomes and comparing them to experimental data. Good matching is also possible with PM, but the parameter assessment requires more time. Only the NSCD method will now be tested with seismic tests on single-story frames.

4.3. Seismic response of the single-story frames

Fig. 12a presents the plane frame finite element model and the structures parameters are the same as for the previous section. The time step calculation equals 0.001s. With a 2 cm separation gap, collision is detected for seven ground motions (Cadarache 0.25 g and 0.30 g, El Centro 0.4 g and 0.45 g, Northridge 0.3 g and 0.35 g, and Kobe 0.4 g). Table 5 presents for each case the damping coefficients ξ_1 and ξ_2 of both structures, and the number of impacts simulated numerically and detected experimentally. Damping coefficients ξ_1 and ξ_2 between [0.4;0.6]% computed inside a Rayleigh Damping matrix [47] yield the best comparison with the experimental results and e still equals to 0.6.

Table 5
Single-story Structures: Modal damping coefficients and impact occurrences.

Ground motion	ξ_1 - ξ_2 (%)	Number of impacts: Numerical/Experimental
Cadarache 0.25 g	0.6–0.5	9/12
Cadarache 0.30 g	0.6–0.5	8/14
El Centro 0.40 g	0.5–0.5	1/3
El Centro 0.45 g	0.5–0.5	4/5
Northridge 0.30 g	0.4–0.4	2/2
Northridge 0.35 g	0.4–0.4	3/3
Kobe 0.40 g	0.6–0.5	2/2

The Cadarache 0.25 g test is now analysed and presented by Fig. 13. It yields very interesting results, especially considering the important number of impacts for the Cadarache ground motions. Indeed, in this case, the number of impact is high (12) and the simulation with $e = 0.6$ delivered 9 of them, always at right times, which shows the good treatment of the impact of the algorithm. Simulations with $e = 0.2$ and 0.9 did not as good results as $e = 0.6$ in terms of impacts numbers and occurrences. As a matter of fact, even after several collisions and potential sources of divergences, the model outcomes kept matching the real displacements. The figure displays the numerical and experimental comparison in displacements (upper figure) and accelerations peaks due to collisions (lower figure). The six remaining ground motion comparisons are presented in Appendix.

Nine of the first ten impacts happen at the exact right instant, and the only one missing (close to 9s) has a small amplitude compared to the others. Since the accelerations peak from the sensors is small, barely noticeable, it can suggest that the structures simply brushed past each other, barely triggering the sensors. Structure 1 numerical displacements are smaller in amplitude starting at 16s, leading to the two remaining contacts not detected (18s and 22s).

Similar high quality results are observed in the Cadarache 0.30 g test, where the timing of 8 major impacts are correctly matched. Only a few impact events were not captured at the end of the ground motion during free vibration (Figure A.1a). The remaining five ground motions with

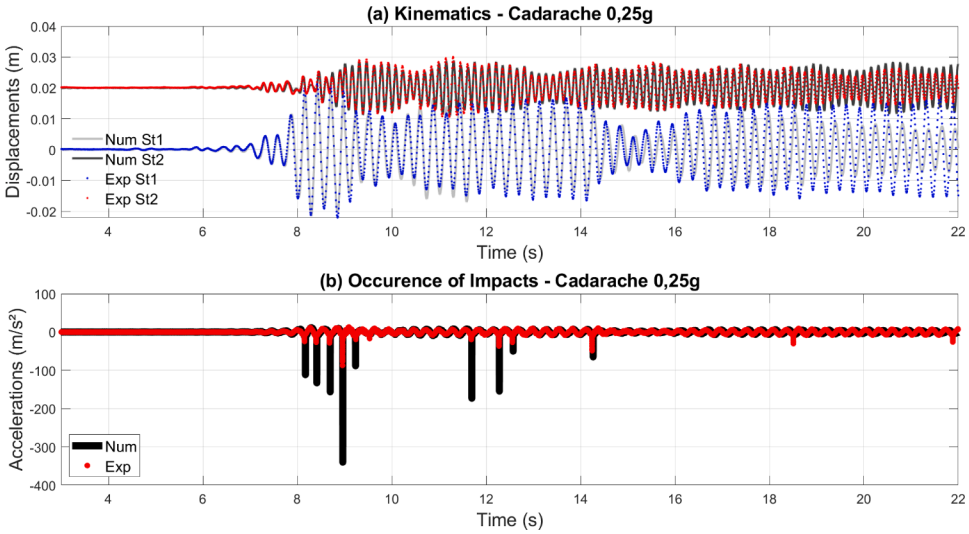

Fig. 13. Single-story results (Cadarache 0.25 g): numerical versus experimental comparison - $e = 0.6$.

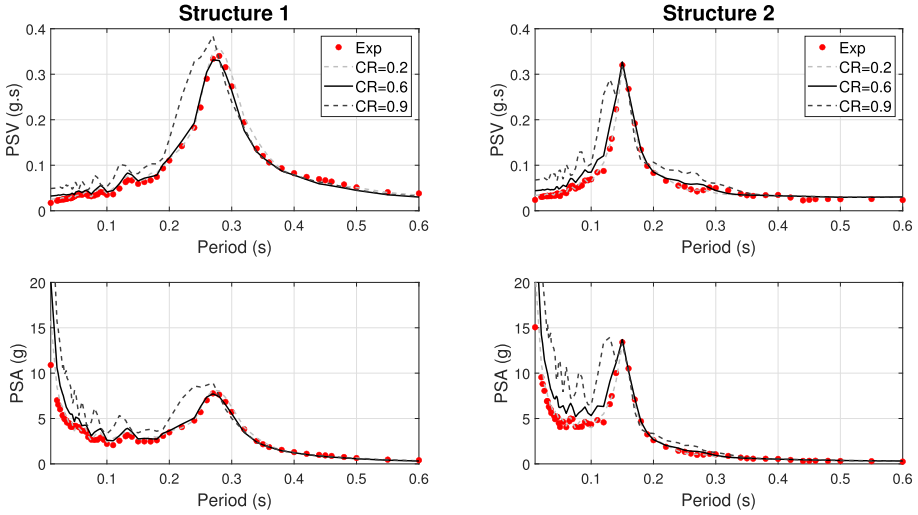

Fig. 14. Single-story: 5% damped Cadarache 0.25 g Spectra with different values of e.

observed impacts (El Centro 0.40 g and 0.45 g, Northridge 0.30 g and 0.35 g, Kobe 0.40 g) are presented in Figs. A.1, A.2, and A.3. Three of them match exactly the number of impacts (Northridge 0.30 g and 0.35 g, Kobe 0.40 g), while the tests for El Centro 0.40 g and El Centro 0.45 g fall short by respectively two and one impacts. Nevertheless, the displacement and frequency responses are matched quite accurately.

Fig. 14 presents the 5% damped pseudo-velocities (PSV) and pseudo-accelerations spectra of Structures 1 and 2. The resemblance of the curves is quite good, and the results are independent on the e values for periods equal and greater than the fundamental periods (0.29s and 0.15s respectively for Structures 1 and Structure 2). For PSV plots, matching is excellent in the full range of periods studied with $e = 0.2$ and 0.6. For PSA plots, matching is better at low periods with $e = 0.2$ (see also Figs. A.3b and A.3d). Furthermore, $e = 0.6$ shows same or better agreement than $e = 0.2$ in Figs. A.1b, A.1d, A.2b, and A.2d.

Overall, taking a constant value of 0.6 for e yields once again good results, both in terms of kinematics and spectral trends for most of the seven different ground motion comparisons (cf. plots in Appendix).

4.4. Seismic response of the two-story frames

For the two-story structures separated by a 5 cm distance, pounding occurred for the following ground motions: Cadarache 0.45 g, El Centro 0.3 g, Northridge 0.2 g, and Kobe 0.2 g and 0.25 g. Because the experimental transverse and torsional eigenfrequencies were available, a 3D-fiber model is used to better model the structures. Figs. 6b and 12b show the real scale and numerical models of the frames respectively. Each structure is composed of fourteen nodes and thirty-two elements. The NSCD method is applied in between the two close corners of each slab so that eight degrees of freedom are involved into the contact detection. The time step calculation is kept at 10^{-3}s. Furthermore, average experimental displacements are obtained from the double integration of the four acceleration piezoelectric sensors on the slab.

Sources of discrepancy:one source of discrepancy comes from the correct evaluation of the damping and modal behaviour. During the experiments, three different tests were carried out to determine the real eigenfrequencies and damping coefficients of each fundamental mode of the structures. They are denoted from the Covariance Driven Stochastic Sub-Space Identification (SSI-COV) white noise analysis, a second one with a decremental logarithmic analysis (SSI-COV (DLA)), and a hammer test. According to Crozet et al. [13], the SSI-COV (DLA) values applied to their own model yielded the best comparisons. Unfortunately, in our case the damping coefficients of the second transverse and torsional modes could not be obtained. As a first approximation, they are

Table 6
Experimental Damping Coefficients ξ from SSI-COV (DLA) test [13].

	1^{st} L. B.	2^{nd} L. B.	1^{st} Tr. B.	2^{nd} Tr. B.	1^{st} To.	2^{nd} To.
ξ (%) Structure 1	0.7	0.2	1.3	**1.3**	2.0	**2.0**
ξ (%) Structure 2	1.0	0.2	1.0	**1.0**	3.0	**3.0**

Table 7
Experimental and Numerical eigenfrequencies.

	1^{st} L. B.	2^{nd} L. B.	1^{st} Tr. B.	2^{nd} Tr. B.	1^{st} To.	2^{nd} To.
Structure 1 Exp (Hz)	2.10	5.60	6.10	17.5	8.60	24.4
Structure 1 Model (Hz)	2.10	5.60	6.11	17.5	8.60	24.4
Structure 2 Exp (Hz)	3.70	10.4	8.20	25.2	10.1	28.0
Structure 2 Model (Hz)	3.69	10.4	8.20	25.2	10.2	28.0

Table 8
Impact occurrences.

Ground motion	Gaps of Left/Right corners (cm)	Number of impacts: Numerical/ Experimental
Cadarache 0.45 g	5/5.5	3/3
El Centro 0.30 g	5/5.5	3/3
Northridge 0.20 g	5.5/6	1/1
Kobe 0.20 g	4.5/5	3/3
Kobe 0.25 g	5/5.5	3/4

taken here equal to the first transverse and torsional coefficient respectively. Eq. (22) presents the expression of the classical damping matrix [47] computed on each structure as the modal superposition of modal damping ratios ξ_n.

$$\mathbf{\Phi_n C \Phi_n^T} = \sum_{n=1}^{J} 2\xi_n \omega_n M_n \tag{22}$$

With J the number of the modes considered in the system response - here six as shown in Table 6; and ω_n, M_n and Φ_n respectively the frequency, the modal mass and the eigenvector corresponding to the n-th mode. This damping matrix enables us to impose each of the six damping ratio to the specified eigenmodes, and have a modal representation of the damping as close as possible to the experimental one.

Table 6 presents the values of damping coefficients finally identified, and Table 7 presents the matching of the numerical eigenfrequencies with the experimental ones. **L. B.**, **Tr. B.**, and **To.** signify respectively the Longitudinal Bending, Transverse Bending, and Torsion modes.

Also, set-up imperfections may create an unplanned motion of the frames. As spotted during the experimental campaign [38,13], the planar surfaces where pounding occurs are not perfectly aligned. The gap separations of the two ends are different, one being 5 cm and the other 5.5 cm. This one important parameter corrupt the experimental kinematic response, creating non-planar and torsional motion. To reproduce the torsional peaks of the experimental pseudo-spectra plots, different separation gaps in the range between 4.0 cm and 6.0 cm were chosen, with a maximum of $\pm$ 0.5 cm difference between the two contact corners gaps.

For the five tests involving pounding, Table 8 displays the asymmetric gap and the number of impacts simulated numerically and detected experimentally. The gaps displayed are the ones, inside the range [4.0;6.0]cm, yielding the best comparison with the experimental results.

The Kobe 0.25 g second floor results are presented here below. The structure response to Cadarache 0.45 g, El Centro 0.30 g, Northridge 0.20 g and Kobe 0.20 g, are included in the Appendix (Figs. A.4 and A.5); the building response and pounding occurrences are in excellent agreement with the measured response as shown in Table 8. Due to the 3D nature of the models, it is possible to plot the displacements of the four facing corners, two of them called “left corners”, and two others “right corners”. For readability, only the displacements and accelerations of the left corner are plotted in Fig. 15.

Fig. 15 shows good agreement of kinematic responses and impact occurrences between experimental and numerical outcomes. One impact was not reproduced at 11s, and by checking the displacements, it was missed only by a few millimeters.

Fig. 16 compares the numerical and measured 5% damped PSV and PSA spectra response for the Kobe 0.25 g ground motion. Herein, the accelerometer data was not averaged to expose the torsional effects are apparent. Overall, the general trends of the curves are well reproduced for all ground motions, especially around 0.48s and 0.27s (the fundamental periods of Structures 1 and 2, respectively). Also, peak

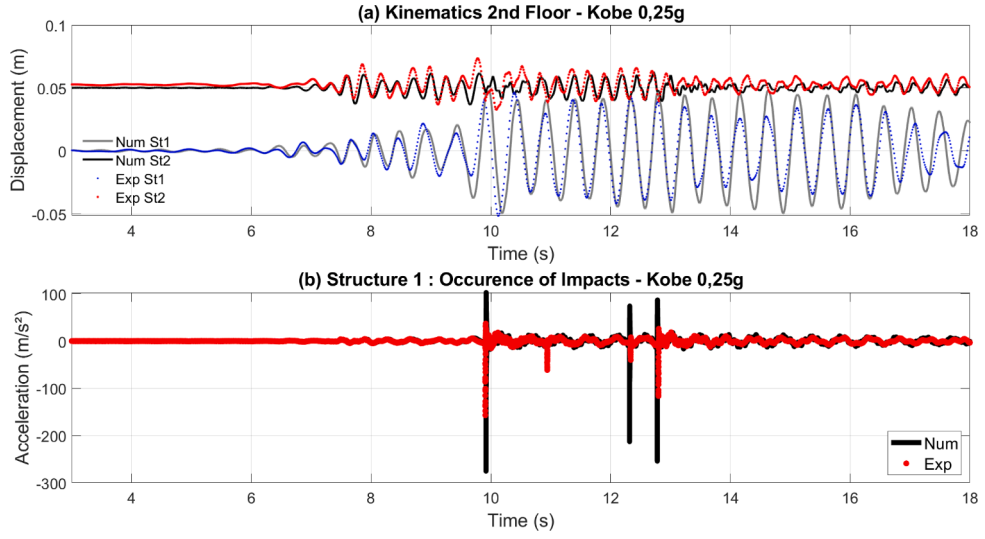

Fig. 15. Two-story results (Kobe 0.25 g): numerical versus experimental comparison.

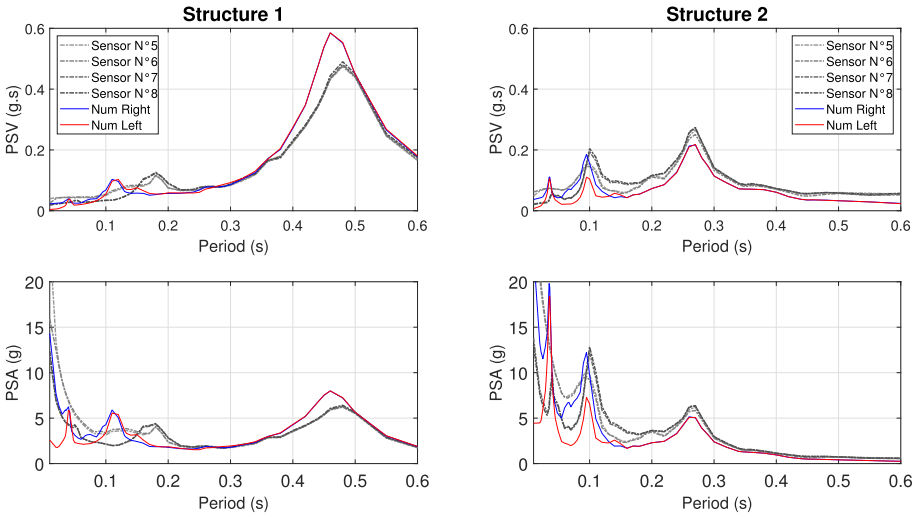

Fig. 16. Two-story (Kobe 0.25 g) Spectra: numerical versus experimental comparison.

amplitudes, especially of PSV, match well the experimental curves for the Kobe 0.25 g as well as for the four other ground motions (see Figures A.4b, A.4d, A.5b, and A.5d). Nevertheless, despite the good kinematics matching, one can notice that the second bending mode of Structure 1 (0.17s) is not apparent as expected.".

5. Discussion

This article presents a numerically efficient algorithm for solving the equations of motion of structural systems subjected to pounding, herein referred to the NSCD method. The algorithm is an implicit Moreau-Jean integration scheme combined with Newton's law of impacts, which relies on the coefficient of restitution e and accounts for energy dissipation upon contact. To illustrate the accuracy and robustness of the NSCD approach, two application examples are presented: (i) a bouncing ball test, and a (ii) building collision test, where NSCD-based solutions are compared with shaking table test results. From this study, the following conclusions can be drawn:

- The NSCD solution to the bouncing ball problem yields the exact analytical solutions, even if larger time steps are used ($\Delta t = 0.001s$ herein). On the other hand, the Penalty Method (PM) yields similar results at the expense of shorter time step and larger computational effort.
- The acceleration obtained from the fundamental theorem of calculus is dependent on the time-step Δt used. The smaller Δt, the higher the amplitude (up to 20 g for Structure 2 in Fig. 16). This point rises reasonable doubt regarding the PSA spectra derived by the NSCD method in building design.
- The NSCD method matched the experimental results very well for the two buildings in terms of amplitude and phase of the displacement histories, as well as timing of pounding events. These observations are valid for the seven single-story structures and the five two-story structures studied. For instance, in the Cadarache 0.25 g test, the numerical model reproduces the displacement history on both structures and the timing of impacts with remarkable accuracy (Nine impacts successfully reproduced, refer to Fig. 13). The 5% response spectra (*e.g.*, PSV, PSA) around the fundamental frequency of each buildings is well captured by the numerical scheme; however, some differences are apparent in higher frequencies. Among several factors, these differences can be attributed to small accidental slab misalignments observed in the experiments, and the inferred modal damping values. These numerical simulations relied on a constant e value, which is also a source of uncertainties.
- A sensitivity analysis was performed and a $e = 0.6$ resulted in very good agreement between the numerical and experimental response. With high quality experimental data, and under the assumption of a constant value for e, this calibration process is straightforward as the number of empirical parameters is significantly reduced. In contrast, finding the correct stiffness coefficient, damping ratio, and integration time step on a PM implementation is cumbersome.

Overall, the NSCD method is a very useful tool for building pounding analyses and a good complement to traditional penalty method approaches. Work is underway to apply NSCD method on inelastic structures and to evaluate the effect of pounding in the context of performance-based design and risk analysis.

Declaration of Competing Interest

The authors declare that they have no known competing financial interests or personal relationships that could have appeared to influence the work reported in this paper.

Acknowledgments

This work is partly founded by an CDSN Grant (Contrat Doctoral Spécifiques aux Normaliens) and the ECOS-Sud Grant for international collaboration CONICYT-ECOS170044.

The authors deeply thanks V. Crozet of the French CEA for the provisioning of the experimental data [13]. Many thanks are also addressed to V. Acary and F. Bourrier respectively of the INRIA (Institut National de la Recherche en sciences et technologies du numérique) and INRAE (Institut National de la Recherche pour l'Agriculture, l'alimentation et l'Environnement) for their guidance into the NSCD method use. In addition, this work has been partially developed within the framework of the federative project I-RISK (L'offre de solutions au traitement des risques naturels) co-funded by the European Union (FEDER) and "La région Auvergne-Rhône-Alpes" which aims at proposing innovative solutions for natural hazards mitigation.

Dr. Candia received support from Facultad de Ingeniería Civil at Universidad del Desarrollo - Chile, FONDECYT Grant 11180937 "Seismic Risk of Mined Tunnels", the National Research Center for Integrated Natural Disaster Management FONDAP/CIGIDEN 15110017, and FONDECYT Grant No. 1170836, "SIBER-RISK: SImulation Based Earthquake Risk and Resilience of Interdependent Systems and NetworKs." The authors are grateful for this support..

Appendix A

See Figs. A.1–A.5.

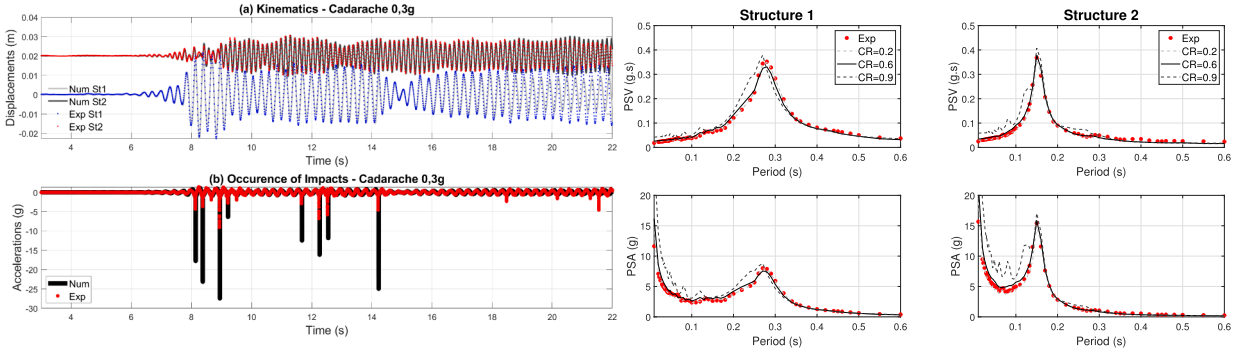

(a) Cadarache 0.30g - Kinematics - e=0.6

(b) Cadarache 0.30g - Spectra

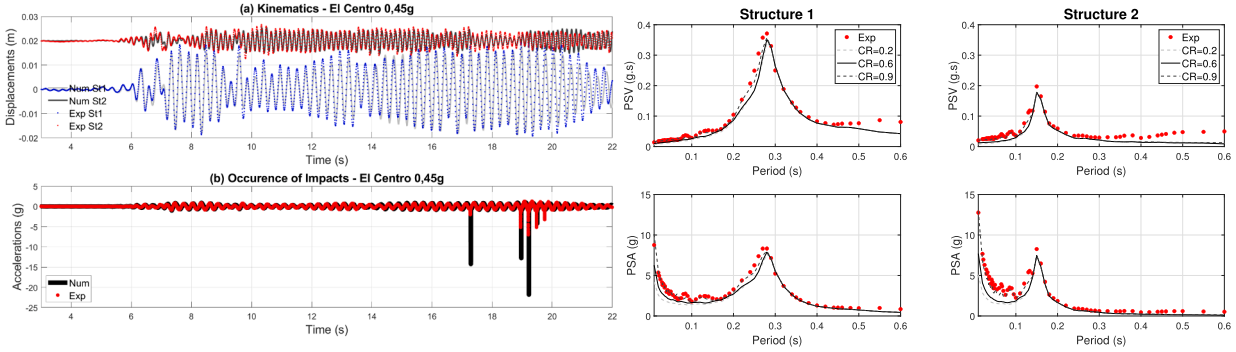

(c) El Centro 0.45g - Kinematics - e=0.6

(d) El Centro 0.45g - Spectra

Fig. A.1. Cadarache 0.30 g and El Centro 0.45 g on single-story structures.

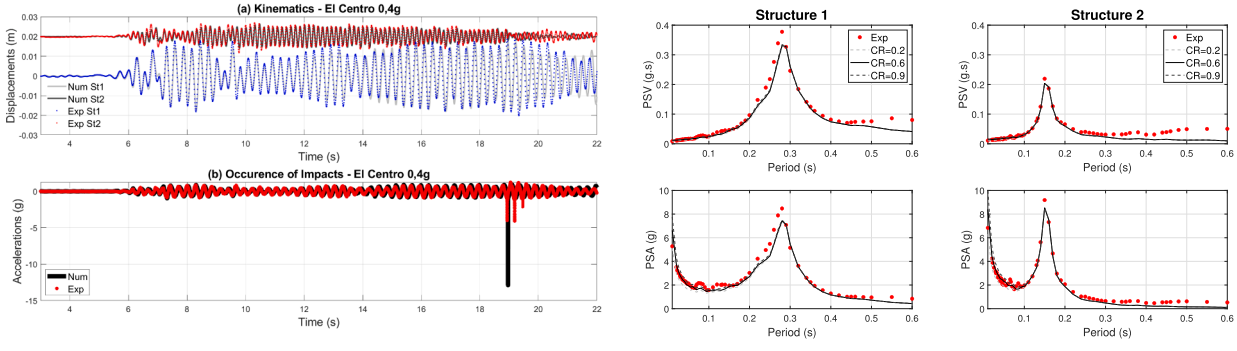

(a) El Centro 0.40g num/exp comparison - e = 0.6

(b) Spectra El Centro 0.40g num/exp comparison

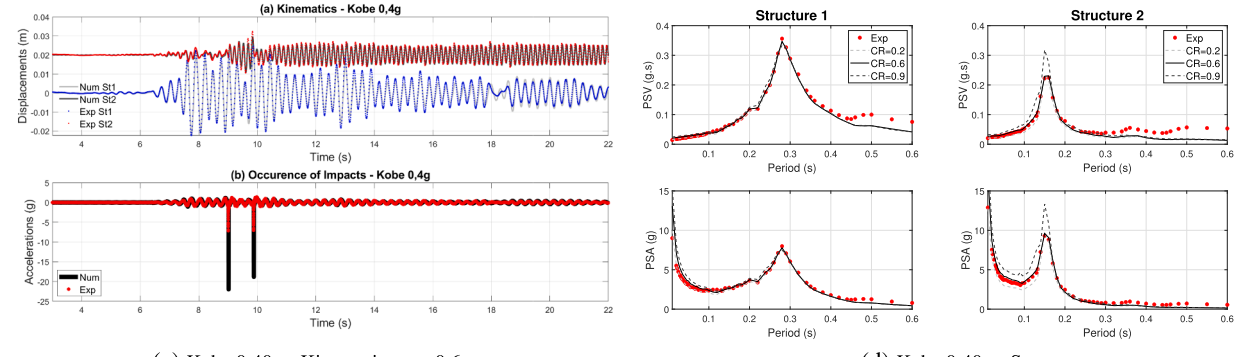

(c) Kobe 0.40g - Kinematics - e=0.6

(d) Kobe 0.40g - Spectra

Fig. A.2. El Centro 0.40 g and Kobe 0.40 g on single-story structures.

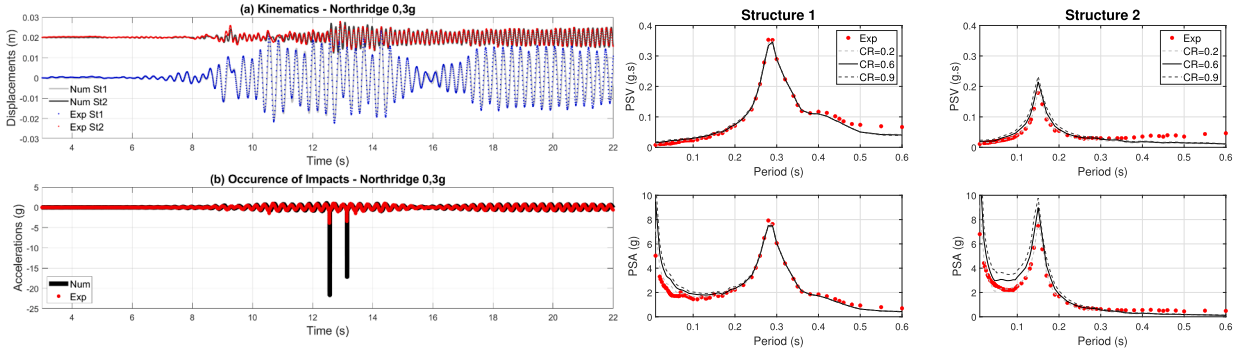

(a) Northridge 0.30g - Kinematics - e=0.6

(b) Northridge 0.30g - Spectra

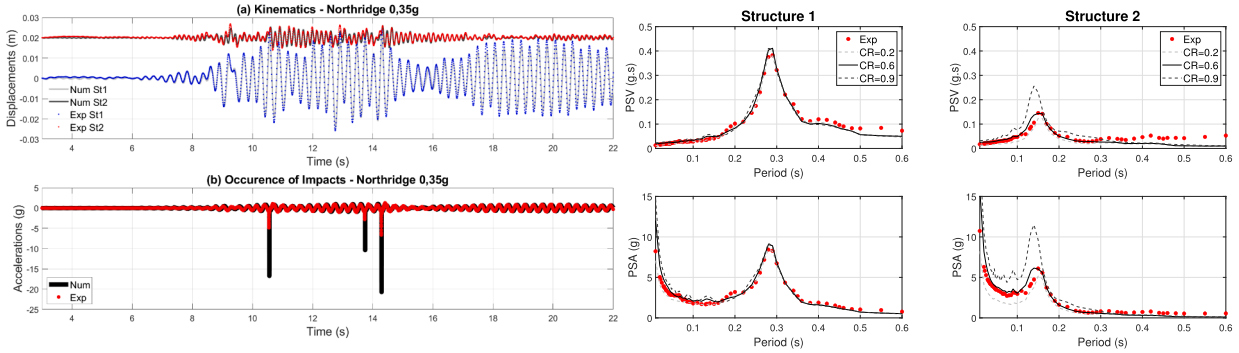

(c) Northridge 0.35g - Kinematics - e=0.6

(d) Northridge 0.35g - Spectra

Fig. A.3. Northridge 0.30 g and 0.35 g on single-story structures.

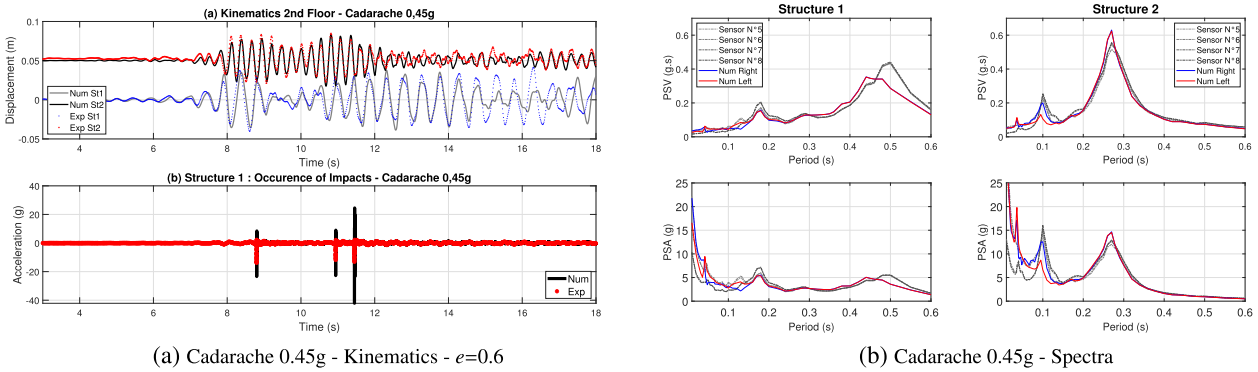

(a) Cadarache 0.45g - Kinematics - e=0.6

(b) Cadarache 0.45g - Spectra

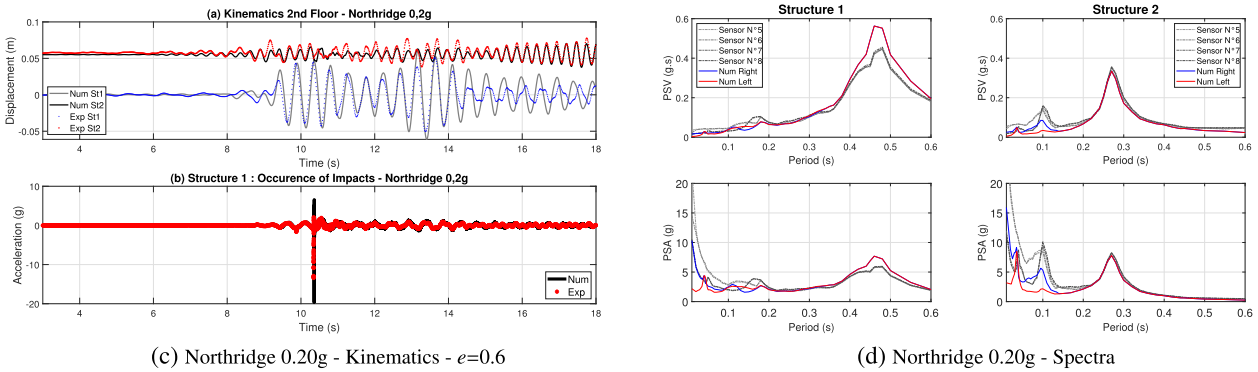

(c) Northridge 0.20g - Kinematics - e=0.6

(d) Northridge 0.20g - Spectra

Fig. A.4. Cadarache 0.45 g and Northridge 0.20 g on two-story structures.

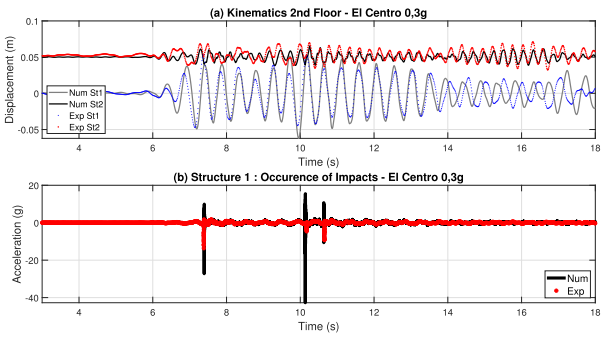

(a) El Centro 0.30g - Kinematics - e=0.6

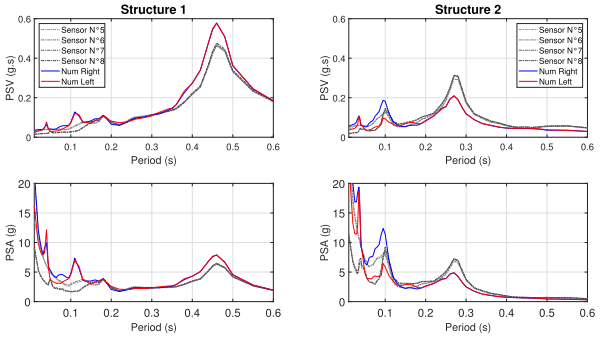

(b) El Centro 0.30g - Spectra

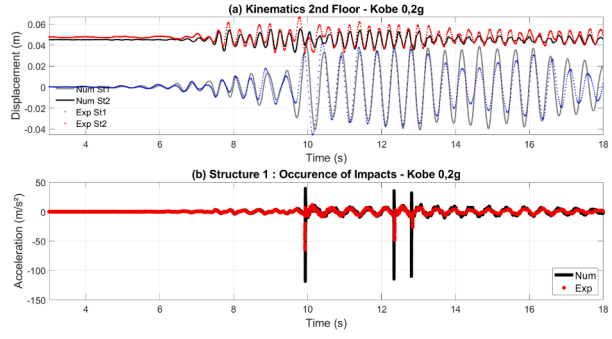

(c) Kobe 0.20g - Kinematics - e=0.6

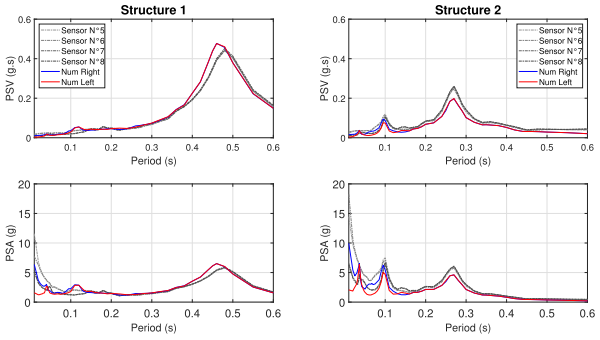

(d) Kobe 0.20g - Spectra

Fig. A.5. El Centro 0.30 g and Kobe 0.20 g on two-story structures.

References

[1] Bertero VV. Observations on Structural Pounding, ASCE, 1987, p. 264–278. URL https://cedb.asce.org/CEDBsearch/record.jsp?dockey=0051055.

[2] Scholl RE. Observations of the performance of buildings during the 1985 Mexico earthquake, and structural design implications. Int J Mining Geolog Eng 1989;7(1): 69–99. https://doi.org/10.1007/BF01552841.

[3] Kasai K, Maison BF. Building pounding damage during the 1989 Loma Prieta earthquake. Eng Struct 1997;19(3):195–207. https://doi.org/10.1016/S0141-0296(96)00082-X. URL http://www.sciencedirect.com/science/article/pii/S014102969600082X.

[4] Reinoso E, Quinde P, Buendía L, Ramos S. Intensity and damage statistics of the September 19, 2017 Mexico earthquake: Influence of soft story and corner asymmetry on the damage reported during the earthquake, Earthquake Spectra, 2021. 87552930209819 81Publisher: SAGE Publications Ltd STM. doi:10.1177/8755293020981981.

[5] Arnold C. Pounding damage at hotel de carlo, The Earthquake Engineering Online Archive NISEE e-Library. https://nisee.berkeley.edu/elibrary/Image/201307115.

[6] Sezen H. Note effect on pounding. The Earthquake Engineering Online Archive NISEE e-Library. https://nisee.berkeley.edu/elibrary/Image/IZT-484.

[7] Jeng V, Tzeng WL. Assessment of seismic pounding hazard for Taipei City. Eng Struct 2000;22(5):459–71. https://doi.org/10.1016/S0141-0296(98)00123-0. URL http://www.sciencedirect.com/science/article/pii/S0141029698001230.

[8] Karayannis CG, Favvata MJ. Earthquake-induced interaction between adjacent reinforced concrete structures with non-equal heights. Earthq Eng Struct Dyn 2005; 34(1):1–20.

[9] Karayannis CG, Naoum MC. Torsional behavior of multistory RC frame structures due to asymmetric seismic interaction. Eng Struct 2018;163:93–111. https://doi.org/10.1016/j.engstruct.2018.02.038. URL http://www.sciencedirect.com/science/article/pii/S0141029617323659.

[10] Bertero VV. Implications of observed pounding of buildings on seismic code regulations. In: 11th World Conference on Earthquake Engineering, 1996.

[11] B. European Committee for Standardization. Design of structures for earthquake resistance. part 1: General rules, seismic actions and rules for buildings. en 1998-1, Eurocode 8.

[12] A.S. of Civil Engineers. Asce standard-asce/sei 7–16: Minimum design loads for buildings and other structures, ASCE.

[13] Crozet V. Etude de l'entrechoquement entre bâtiments au cours d'un séisme, These de doctorat, Institut polytechnique de Paris (Nov. 2019). URL http://www.theses.fr/2019IPPAE002.

[14] Favvata MJ. Minimum required separation gap for adjacent RC frames with potential inter-story seismic pounding. Eng Struct 2017;152:643–59. https://doi.org/10.1016/j.engstruct.2017.09.025. URL https://linkinghub.elsevier.com/retrieve/pii/S0141029617304509.

[15] Elwardany H, Seleemah A, Jankowski R. Seismic pounding behavior of multi-story buildings in series considering the effect of infill panels. Eng Struct 2017;144: 139–50. https://doi.org/10.1016/j.engstruct.2017.01.078. URL https://linkinghub.elsevier.com/retrieve/pii/S0141029616305107.

[16] Favvata MJ, Naoum MC, Karayannis CG. Limit states of RC structures with first floor irregularities. Struct Eng Mech 2013;47(6):791–818. https://doi.org/10.12989/sem.2013.47.6.791. https://www.koreascience.or.kr/article/JAKO201332251648361.page.

[17] Karayannis CG, Favvata MJ, Kakaletsis DJ. Seismic behaviour of infilled and pilotis RC frame structures with beam-column joint degradation effect. Eng Struct 2011; 33(10):2821–31. https://doi.org/10.1016/j.engstruct.2011.06.006. URL http://www.sciencedirect.com/science/article/pii/S0141029611002410.

[18] Anagnostopoulos S. Pounding of buildings in series during earthquakes. Earthq Eng Struct Dyn 1988;16:443–56.

[19] Anagnostopoulos S. Building pounding re-examined: How serious a problem is it?. In: 11th World Conference on Earthquake Engineering, 1996.

[20] Anagnostopoulos S. Equivalent viscous damping for modeling inelastic impacts in earthquake pounding problems. Earthq Eng Struct Dyn. doi:10.1002/eqe.377).

[21] Jankowski R. Analytical expression between the impact damping ratio and the coefficient of restitution in the non-linear viscoelastic model of structural pounding. Earthq Eng Struct Dyn. 2006;35(4): 517–24, _eprint: https://onlinelibrary.wiley.com/doi/pdf/10.1002/eqe.537. doi: 10.1002/eqe.537. https://onlinelibrary.wiley.com/doi/abs/10.1002/eqe.537.

[22] Jankowski R. Comparison of Numerical Models of Impact Force for Simulation of Earthquake-Induced Structural Pounding. In: Bubak M, van Albada GD, Dongarra J, Sloot PMA, editors. Computational Science - ICCS 2008. Lecture Notes in Computer Science. Berlin, Heidelberg: Springer; 2008. p. 710–7. https://doi.org/10.1007/978-3-540-69384-076.

[23] Jankowski R. Non-linear viscoelastic modelling of earthquake-induced structural pounding. 2005; 17.

[24] Jankowski R, Mahmoud S. Earthquake-Induced Structural Pounding, GeoPlanet: Earth and Planetary Sciences. Springer International Publishing; 2015. https://doi.org/10.1007/978-3-319-16324-6. URL https://www.springer.com/gp/book/9783319163239.

[25] Naderpour H, Barros RC, Khatami SM, Jankowski R. Numerical study on pounding between two adjacent buildings under earthquake excitation, iSSN: 1070-9622 Pages: e1504783 Publisher: Hindawi Volume: 2016 (Jan. 2016). doi:https://doi.org/10.1155/2016/1504783. URL https://www.hindawi.com/journals/sv/2016/1504783/.

[26] Xu X, Xu X, Liu W, Zhou D. A new formula of impact stiffness in linear viscoelastic model for pounding simulation, iSSN: 1070-9622 Pages: e5861739 Publisher: Hindawi Volume: 2016 (Sep. 2016). doi:https://doi.org/10.1155/2016/5861739. URL https://www.hindawi.com/journals/sv/2016/5861739/.

[27] Papadrakakis M, Mouzakis H, Plevris N, Bitzarakis S. A lagrange multiplier solution method for pounding of buildings during earthquakes. Earthq Eng Struct Dyn 1991; 20(11):981–98. https://doi.org/10.1002/eqe.4290201102. _eprint: https://onlinelibrary.wiley.com/doi/pdf/10.1002/eqe.4290201102, URL https://onlinelibrary.wiley.com/doi/abs/10.1002/eqe.4290201102.

[28] Mouzakis HP, Papadrakakis M. Three dimensional nonlinear building pounding with friction during earthquakes. J Earthq Eng 2004;08(01):107–32. https://doi.org/10.1142/S1363246904001353. publisher: Imperial College Press. https://www.worldscientific.com/doi/abs/10.1142/S1363246904001353.
[29] Cole GL. The effects of detailed analysis on the prediction of seismic building pounding performance, Ph.d thesis, University of Canterbury, accepted: 2013-10-02T01:16:38Z Publisher: University of Canterbury. Department of Civil and Natural Resources Engineering, 2012. doi:10.26021/2867. URL https://ir.canterbury.ac.nz/handle/10092/8384.
[30] Ambiel J, Brun M, Faye P, Thibon A, Gravouil A. Entrechoquement entre des structures en béton armé soumises à un chargement sismique, 14ème Colloque National en Calcul des Structures (CSMA), 2019.
[31] Cole G, Dhakal RP, Carr AJ, Bull D. Building pounding state of the art: Identifying structures vulnerable to pounding damageAccepted: 2010-09-02T21:28:05Z Publisher: University of Canterbury. Civil and Natural Resources Engineering. https://ir.canterbury.ac.nz/handle/10092/4445.
[32] Candia G, Llera JCdl, Almazán JL. A physical model for dynamic analysis of wine barrel stacks. Earthq Eng Struct Dyn 2010;39(10):1063–81. https://doi.org/10.1002/eqe.979. _eprint: https://onlinelibrary.wiley.com/doi/pdf/10.1002/eqe.979. https://onlinelibrary.wiley.com/doi/abs/10.1002/eqe.979.
[33] Hertz H. Ueber die Ausbreitungsgeschwindigkeit der electrodynamischen Wirkungen. Annalen der Physik 1888;270(7):551–69. https://doi.org/10.1002/andp.18882700708. _eprint: https://onlinelibrary.wiley.com/doi/pdf/10.1002/andp.18882700708. https://onlinelibrary.wiley.com/doi/abs/10.1002/andp.18882700708.
[34] Goldsmith W. Impact: the Theory and Physical Behaviour of Colliding Solids, E. Arnold, 1960, google-Books-ID: nxAIAQAAIAAJ.
[35] Ye K, Li L, Zhu H. A modified Kelvin impact model for pounding simulation of base-isolated building with adjacent structures. Earthq Eng Eng Vib 2009;8(3):433–46. https://doi.org/10.1007/s11803-009-8045-4.
[36] Khatami SM, Naderpour H, Barros RC, Jakubczyk-Galczynska A, Jankowski R. Effective formula for impact damping ratio for simulation of earthquake-induced structural pounding. Geosciences 2019;9(8):347. https://doi.org/10.3390/geosciences9080347. number: 8 Publisher: Multidisciplinary Digital Publishing Institute. https://www.mdpi.com/2076-3263/9/8/347.
[37] Crozet V, Politopoulos I, Yang M, Martinez J-M, Erlicher S. Sensitivity analysis of pounding between adjacent structures. Earthq Eng Struct Dyn 2018;47(1):219–35. https://doi.org/10.1002/eqe.2949. _eprint: https://onlinelibrary.wiley.com/doi/pdf/10.1002/eqe.2949. https://onlinelibrary.wiley.com/doi/abs/10.1002/eqe.2949.
[38] Crozet V, Politopoulos I, Chaudat T. Shake table tests of structures subject to pounding. Earthq Eng Struct Dyn 2019;48(10):1156–73. https://doi.org/10.1002/eqe.3180. _eprint: https://onlinelibrary.wiley.com/doi/pdf/10.1002/eqe.3180. https://www.onlinelibrary.wiley.com/doi/abs/10.1002/eqe.3180.
[39] Khatiwada S, Chouw N. Limitations in simulation of building pounding in earthquakes. Int J Protective Struct 2014;5(2):123–50. https://doi.org/10.1260/2041-4196.5.2.123. publisher: SAGE Publications.
[40] Acary V, Brogliato B. Numerical methods for nonsmooth dynamical systems: applications in mechanics and electronics. Springer; 2008.
[41] Acary V. Projected event-capturing time-stepping schemes for nonsmooth mechanical systems with unilateral contact and Coulomb's friction. Comput Methods Appl Mech Eng 2013;256:224–50. https://doi.org/10.1016/j.cma.2012.12.012. URL http://www.sciencedirect.com/science/article/pii/S0045782512003829.
[42] Moreau JJ. Standard inelastic shocks and the dynamics of unilateral constraints. In: Del Piero G, Maceri F, editors. Unilateral problems in structural analysis, international centre for mechanical sciences. Vienna: Springer; 1985. p. 173–221. https://doi.org/10.1007/978-3-7091-2632-59.
[43] Jean M. The non-smooth contact dynamics method. Comput Methods Appl Mech Eng 1999;177(3-4):235–57. https://doi.org/10.1016/S0045-7825(98)00383-1. URL https://hal.archives-ouvertes.fr/hal-01390459.
[44] Acary V. Energy conservation and dissipation properties of time-integration methods for nonsmooth elastodynamics with contact. ZAMM - J Appl Mathe Mech/Zeitschrift für Angew Mathematik Mechanik 2016;96(5):585–603. https://doi.org/10.1002/zamm.201400231. _eprint: https://onlinelibrary.wiley.com/doi/pdf/10.1002/zamm.201400231. https://onlinelibrary.wiley.com/doi/abs/10.1002/zamm.201400231.
[45] Acary V. Contribution à la modélisation mécanique et numérique des édifices maçonnés, phdthesis, Université de la Méditerranée - Aix-Marseille II (May 2001). URL https://tel.archives-ouvertes.fr/tel-00163767.
[46] Jankowski R. Experimental study on earthquake-induced pounding between structural elements made of different building materials. Earthq Eng Struct Dyn 2010;39(3):343–54. https://doi.org/10.1002/eqe.941. _eprint: https://onlinelibrary.wiley.com/doi/pdf/10.1002/eqe.941. https://onlinelibrary.wiley.com/doi/abs/10.1002/eqe.941.
[47] Chopra AK. Dynamics of structures. 4th ed. Upper Saddle River, N.J.: Pearson; 2011.